
1 **Quantitative characterization of three-dimensional pore structure in**
2 **hardened cement paste using X-ray microtomography combined with**
3 **centrifuge driven metal alloy intrusion**

4 Rusheng Qian¹, Yunsheng Zhang^{1,*}, Cheng Liu², Lin Yang³, Guojian Liu¹, Wei She¹

5 ¹ Jiangsu Key Laboratory for Construction Material, Southeast University, Nanjing 211189,
6 China

7 ² Advanced and Innovative Materials (AIM) Group, Department of Civil, 12 Environmental
8 and Geomatic Engineering, University College London, London 13 WC1E 6BT, UK)

9 ³ School of Water Conservancy and Environment, Zhengzhou University, Zhengzhou 450001,
10 China

11 **Abstract**

12 In this paper, a centrifuge device is proposed to facilitate the intrusion of a
13 low-melting point metal alloy into the pore space of hardened cement paste. X-ray
14 microtomography is combined with metal centrifugation porosimetry (MCP) to
15 quantitatively investigate 3D pore structure. The low-melting-point metal alloy is
16 melted and introduced into pore space in pastes with water cement ratio of 0.5 and 1.0
17 at a temperature of 65°C. 3D pore structure is quantitatively analyzed by X-ray
18 microtomography after the molten metal alloy has been consolidated. A new threshold
19 value segmentation method for pore space was proposed using conversion coefficient
20 on region of interest (ROI). Porosity and pore size distribution are tested by MCP and
21 compared with the results based on mercury intrusion porosimetry (MIP). The results
22 show that the contrast between pore space and solid phase in the X-ray
23 microtomography device image is improved. The total porosity obtained by MCP was
24 found to be consistent with the results obtained by MIP.

25 **Keywords:** X-ray microtomography; Porous material; 3D pore structure;
26 Quantitative characterization; Cement

27 **1. Introduction**

28 Cement-based materials are considered as one of the most vital materials, as
29 they play an important role in infrastructure development^[1]. These materials consist
30 of liquid, solid and gas phases whose properties are strongly correlated with the
31 performance of modern concrete^[2, 3]. Porosity in cement-based materials is directly

Corresponding author: Zhang Yunsheng
Jiangsu Key Laboratory for Construction Material, Southeast University, Nanjing 211189, China
E-mail: zhangys279@163.com

32 associated with the mechanical performance as well as transport properties ^[4]. Hence,
33 quantitative characterization of pore structure of cement-based materials is important
34 to assess the performance of concrete ^[5].

35 Several commonly used techniques are available for characterization of pore
36 structure in cement-based materials, including small-angle X-ray scattering,
37 Brunaures-Emmitt-Teller adsorption and mercury intrusion porosimetry(MIP) ^[6].
38 Among them, MIP technique is the most widely employed technique in research due
39 to its advantages such as large dynamic range of pore size characterization (from a
40 few nanometers to a few hundred micrometers), high performance and short testing
41 durations. However, this method has limited applications due to the ink bottle effect ^[7]
42 and it assumes cylindrical pore geometry ^[8]. Due to these assumptions, the estimation
43 of pore parameters such as porosity, pore connectivity and surface-to-volume ratio by
44 the MIP method are inaccurate. Moreover, the detailed topology of 3D pore structure
45 has not be obtained until now, which is crucial to the performance in cement-based
46 materials. Although, scanning electron microscopy (SEM) has been conventionally
47 applied to analyze pore structure as it offers a high resolution, the low contrast
48 between pore space and solid phase limits the information of pore structure to 2D
49 only.

50 As a well-established technology, X-ray computed tomography (X-ray CT) can
51 achieve the visualization of 3D pore structure ^[9]. However, current results mostly
52 focused on pore structure of concrete with larger pore size, such as foamed concrete
53 ^[10, 11] and cracked concrete ^[12] due to high contrast between pore space and solid
54 phase. The limited application of X-CT in common or high performance concrete are
55 mainly due to the fact that the threshold value between pore space and solid phase in
56 CT slice figure is not obvious arising from relatively low attenuation. Therefore the
57 classification of threshold value is subjective ^[13]. In order to reduce subjectivity,
58 contrast agents have been applied in porosity characterization of porous material, such
59 as Wood's metal ^[14-18], polymethylmethacrylate (PPMA) ^[19] and mercury^[20]. Pore
60 structure ^[14-16] was analyzed only on 2D using Wood's metal combined with high
61 pressure. Wood's metal was also used in clay rock ^[17] to obtain 3D structure of
62 materials combined with focused ion beam (FIB). PPMA ^[19] and mercury ^[20] were
63 applied to research pore structure in crystalline rock with ordinary CT imaging. In
64 addition, the resolution of ordinary X-ray CT and micro X-ray CT used are not
65 enough for micro pore scale research ^[21]. Hence there is need for techniques that have
66 a high contrast and a high precision to image 3D pore structures in cement-based

67 materials.

68 In this study, a novel contrast enhanced X-ray microtomography technique has
69 been employed for the first time to quantitatively characterize 3D pore structure in
70 cement pastes. A new threshold value segmentation method for pore space was
71 proposed based on ROI combined with volume compensation factor. The metal alloy
72 is centrifuged into pore spaces to enhance their contrast in X-ray microtomography
73 images.

74 2. Materials and methods

75 2.1 Materials and instrumentation

76 2.1.1 Preparations of specimen

77 The cement used in this study is a Chinese standard Graded P•II 52.5 type
78 Portland cement with a density of 3150 kg/m³ and specific surface area of 369.60
79 m²/kg. Its chemical composition is listed in Table. 1. It has an initial and final setting
80 time of 132 min and 187 min, respectively. Its compression and flexural strength for a
81 28 day curing duration under standard conditions are 59.60 MPa and 9.20 MPa,
82 respectively.

83

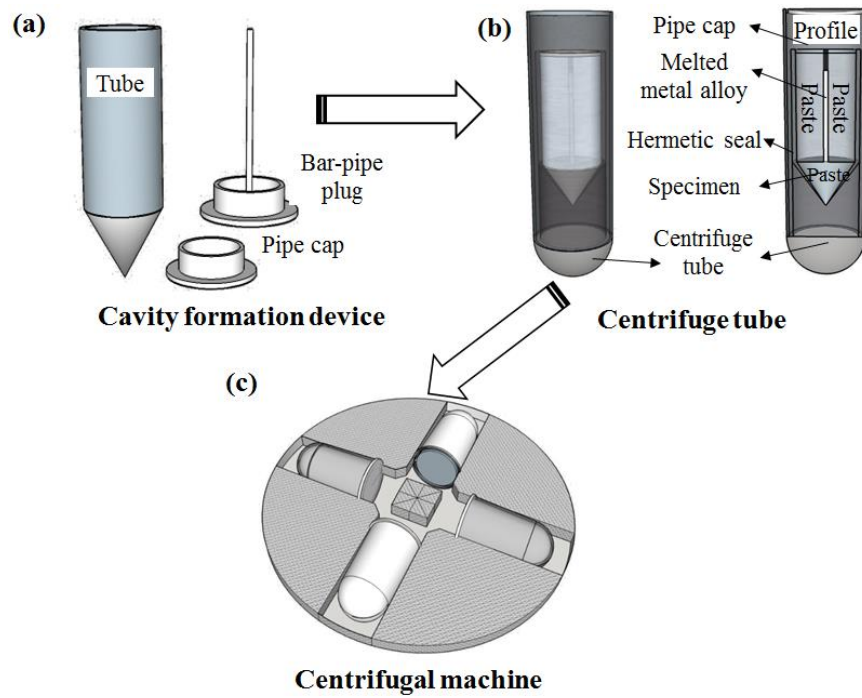
84 Table 1

85 Chemical composition of cement

Cement	Chemical composition (%)								
	SiO ₂	Al ₂ O ₃	Fe ₂ O ₃	CaO	MgO	SO ₃	Na ₂ O	K ₂ O	LOI
Content	21.35	4.67	3.31	62.60	3.08	2.25	0.11	0.65	0.95

86

87 Cement pastes were prepared with water cement ratio (w/c) of 0.5 and 1.0.
88 Cavity formation was facilitated in the prepared specimens to hold the molten metal
89 using the proposed device, as shown in Fig. 1(a). Firstly, the fresh cement paste was
90 poured into the tube and then pressed down the bar-pipe plug to produce the cavity.
91 Then, the samples were put into a rotating device to constantly and slowly rotate up
92 and down during the whole setting and hardening time of the fresh cement paste.
93 After the setting and hardening of the paste, the bar-pipe plug was dialed out carefully
94 and replaced with the pipe cap, curing paste at 20±1 °C/95% RH for 28 d and 14 d
95 (Table. 2). Finally, the specimens were soaked in ethyl alcohol for 3 d to terminate
96 hydration and dried at a temperature of 65 °C in the air oven until mass constancy to
97 exclude gas in pores of the hardened cement paste.



99

100 Fig. 1 Schematics of the proposed centrifugal device design. (a) Cavity formation device, (b)
 101 Thermal-insulation centrifuge tube and (c) Centrifuge machine

102

103 Table 2

104 Sample information

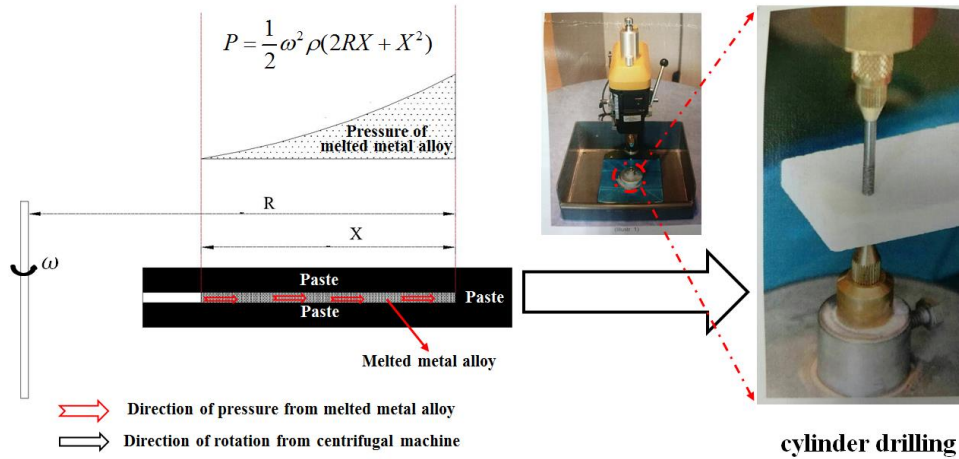
Sample name	w/c	Age (days)	Centrifuge Speed (RPM)	Intrusion Pressure (MPa)
Untreated	0.5	28	4000	12.02
A	0.5	28	4000	12.02
B	0.5	14	4000	12.02
C	1.0	14	4000	12.02

105

106 2.1.2 Proposed centrifuge device design

107 The experimental set-up used to intrude the metal into the sample consisted of an
 108 in-house developed thermal-insulation centrifuge tube (Fig. 1(b)) and a centrifuge
 109 machine (maximum speed: 4000 r/min) (Fig. 1(c)). Firstly, the molten metal alloy was
 110 injected into the cavity of sample. Then, the sample was tightly and hermetically
 111 coated with extruded polystyrene (heat conductivity coefficient 0.030 W/ (m K)) to
 112 maintain the experiment time (65°C). Finally, the sample was placed in a centrifuge
 113 tube to be subjected to the centrifugal process at 4000 r/min for 30 min. Subsequently,

114 the specimen was cooled below 47°C, after which a cylinder with diameter of 1.0 mm
 115 was drilled for X-ray microtomography (Fig. 2). Three samples (A, B, C) were
 116 prepared under the conditions and one untreated sample was prepared under the same
 117 formation and curing conditions for control group, as listed in Table.2.
 118



119
 120 Fig. 2 Cylinder drilling for MCP testing

121 2.1.3 Metal alloy properties

122 The metal alloy used in this experiment has a chemical composition of 43.7%Bi,
 123 20.6%Pb, 8.6%Sn, 5.8%Cd, 20.1%In and other trace elements (tested by X Ray
 124 Fluorescence), which is similar to Bismuth alloy^[22] as shown in table 3. The metal
 125 alloy has a melting point of 47°C and a specific gravity of 9.4 g/cm³. Compared with
 126 Wood's metal ^[23], the metal alloy has lower Lead, lower Cadmium and extra Indium.
 127 Although the volume change of the metal alloy on crystallization was not
 128 experimentally determined, an estimate of 0.0057 mm/mm expansion for a 500 h
 129 post-casting duration was considered for a similar metal ^[24]. The metal alloy-cement
 130 paste contact angle changed with temperature between 110°~130°(tested by high
 131 temperature vacuum contact Angle tester), which is close to the mercury-paste contact
 132 angle (117°~140°) ^[25], as shown in the Fig. 3. In order to facilitate energy-saving and
 133 avoiding decomposition of ettringite in hydration products, a temperature of 65°C
 134 was chosen for the experiment. The surface tension of the metal alloy was
 135 σ=0.508N/m at a temperature of 65°C.

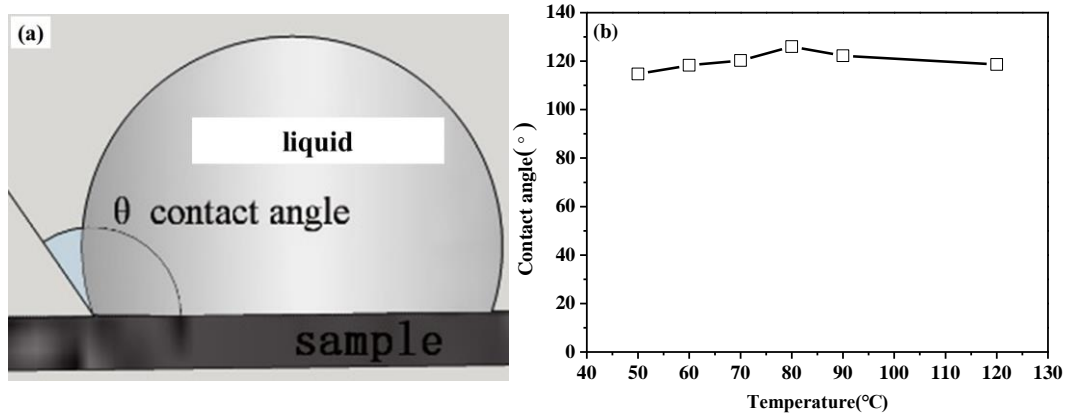


Fig. 3 (a) Diagram of contact angle, (b) Contact angle between the metal alloy and the cement paste as a function of temperature

Table 3

Chemical composition of cement

	Composition by weight	Melting point	Density(g/cm ³)
The metal alloy	43.7%Bi, 20.6%Pb, 8.6%Sn, 5.8%Cd, 20.1%In	47°C	9.40
Bismuth alloy ^[1]	44.7%Bi, 22.6%Pb, 11.3%Sn, 5.3%Cd, 16.1%In ^[22]	47-52°C ^[22]	9.16 ^[22]
Wood's metal ^[2]	50.0% Bi, 26.7% Pb, 13.3% Sn, 10.0% Cd ^[23]	70°C ^[23]	9.38 ^[23]

2.1.4 Experimental parameters

In this study, the model of X-ray microtomography scanner was Y.CT Precision (Zeiss, Germany) and the type of detector was Y.XRD 1601. The intensity of the X-ray beam after sample penetration was measured by 1024 detectors. The voltage and current of X-ray tube was 40 kV and 75 μ A. The rotation angle of sample platform was 360° and increment of rotated samples was 0.0010rad. A tray was placed on the sample platform and a support device was placed at the top of the tray. All samples were scanned at the same station using the X-ray microtomography over 5 hour scanning time, and images with a pixel size of 1 μ m were reconstructed using VGStudio MAX software.

The metal alloy-paste contact angle was measured by high temperature vacuum contact Angle tester (Dataphysics, OCA25HTV). Solid metal alloy was heated into molten metal alloy in the temperature of 65°C and dripped to the surface of paste, then the contact angle was measured subsequently. The MIP tests were done on Autopore

157 IV9510 (Micromeritics) with a low pressure of 0.53 psia mercury filling pressure and
158 maximum intrusion pressure of 60000.00 psia.

159 **2.2 Centrifuge intrusion procedure**

160 Due to capillary action and a favorable contact angle between the molten metal
161 and paste, an external force can drive the molten metal into the pore space [25]. Other
162 factors such as the density of the metal, the speed of the centrifuge device and the
163 centrifugal radius are also relevant. For the proposed device, the intrusion pressure P
164 can be calculated as (Fig. 2),

$$165 \quad P = \frac{1}{2} \omega^2 \rho (2RX + X^2) \quad (1)$$

166 Where, ω is the centrifuge speed, whose unit is rad/s, $\rho=9.4 \text{ g/cm}^3$ is the density
167 of the molten metal alloy, $R=48.0 \text{ mm}$ is the distance from the center of centrifuge to
168 the surface of molten metal in the tube, $X=82.0 \text{ mm}$ is the depth of molten metal
169 alloy to the upper surface of the cement sample.

170 The corresponding pore size is derived based on Washburn's equation [21] as,

$$171 \quad p = -\frac{4\sigma \cos \theta}{d} \quad (2)$$

172 Where, $\sigma=0.508\text{N/m}$, $\theta=110^\circ\sim 130^\circ$ (here $\theta=120^\circ$ was chosen), when $P=12.02\text{MPa}$
173 (Table 2), the result of d is $0.085 \mu\text{m}$, which means that the minimum capillary pore
174 radius can be invaded by the molten metal alloy using the experimental set-up.

175 **2.3 Segment pore methods**

176 In this study, threshold value was significant to segment pores from the base
177 material and to calculate porosities and the pore size distributions. Due to
178 overlapping greyscale part of the metal alloy and treated samples, it's essential to
179 reasonably choose region of interest (ROI) where embrace the vast majority of the
180 metal alloy but very little untreated sample greyscale. Pixel ratio on ROI was
181 counted for treated samples, which named incipient porosity (P_i). And pixel ratio of
182 the metal alloy on ROI was volume compensation factor, which named conversion
183 coefficient (μ). Then, actual porosity (P_a) can be calculated as,

$$184 \quad P_a = \frac{P_i}{\mu} \quad (3)$$

185 Finally, the threshold value of sample was determined based on ROI. Porosity
186 based on the threshold value was calculated again, which named P_t . The threshold

187 value could be constantly adjusted until P_t was very close to P_a . Thereby, pore
188 structure can be reconstructed based on ultima threshold value and pore size
189 distributions can be calculated in one fixed direction.

190 **3. Results and discussion**

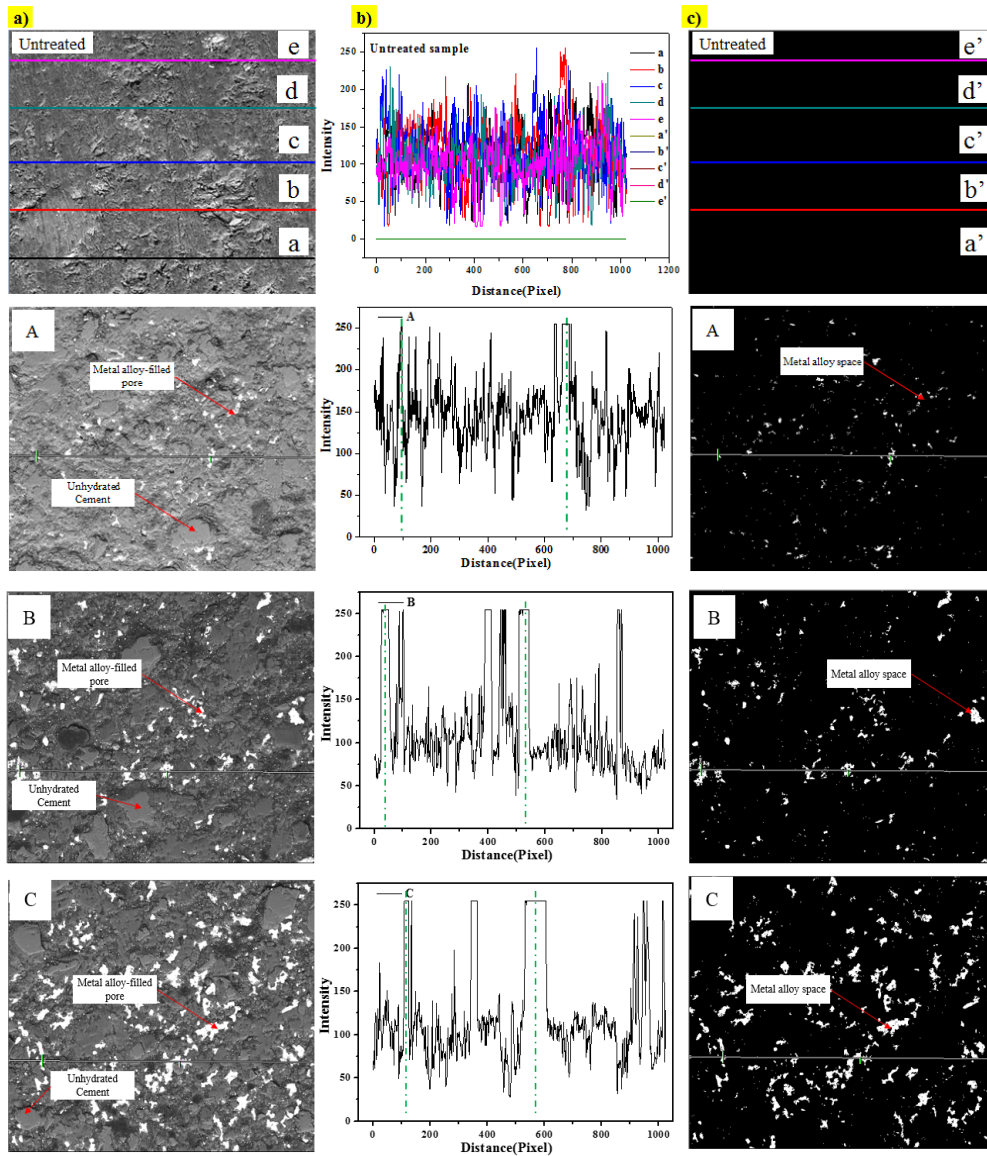
191 The different phases in the samples could be seen with improved contrast since
192 the atomic number of elements in the cement pastes (Si, Ca, O, Al, etc.) was lower
193 than the metal alloy constituents (43.7%Bi, 20.6%Pb, 8.6%Sn, 5.8%Cd, 20.1%In, etc.)
194 in the pores. The high gray values (brightness) in the image indicated that the molten
195 metal alloy was favorably intruded into the pore structure [26]. Appropriate image
196 thresholding was performed to highlight the metal zone and to calculate the porosity
197 and pore size distribution of the specimens.

198 **3.1 SEM images**

199 As shown in Fig. 4 a), the SEM images of sample A, B and C were compared
200 with untreated sample. The areas of high brightness show the zone of pore structure
201 occupied with the metal alloy. In order to determine pore space, firstly, straight line
202 was chosen to across the SEM image of samples and intensity (gray value 0~255) was
203 shown using 'Line Profile' of Image-Pro Plus software, as demonstrated in Fig. 4 b).
204 Little or no intensities of untreated sample reached to gray value 255 in spite of 5
205 lines were chosen to parallely across the SEM image. Differently, some intensities of
206 sample A, B and C were reached to gray value 255 because the metal alloy. The
207 reasons are that cement grains surface were completely covered with outproduct in
208 cement hydration [27,28], especially low density C-S-H [29], which lead to more density
209 contrast between cement and the metal alloy. Hence, greyscale 255~255 was
210 considered as ROI in the SEM images. P_i was counted for sample A, B and C as
211 11.41%, 17.73% and 25.32% based on ROI. Pixel ratio of the metal alloy on ROI was
212 calculated as 96.15%, which was the conversion coefficient ($\mu=0.9615$). Therefore, P_a
213 was calculated as 11.87%, 18.44% and 26.33%, respectively. As shown in Fig. c), the
214 threshold values of 251~255, 248~255 and 245~255 were chosen to distinguish the
215 metal alloy (pore space) and cement using segment pore methods when P_t is very
216 close to P_a , as demonstrated in Table 4.

217

218



219

220

221

222

223

224

225

Fig. 4. a) SEM image, b) Intensity to distance, c) The extracting pixels of pores space by Image-Pro Plus software (sample A, B and C based on the grayscale 251~255, 248~255 and 245~255, respectively)

Table 4

Data information

Pore structure	Sample name	Actual porosity P_a (%)	ROI	Conversion coefficient(μ)	Threshold value
2D	A	11.87			251~255
	B	18.44	255~255	0.9615	248~255
	C	26.33			245~255
3D	A	22.74			184~255
	B	27.24	185~255	0.9709	183~255
	C	50.53			180~255

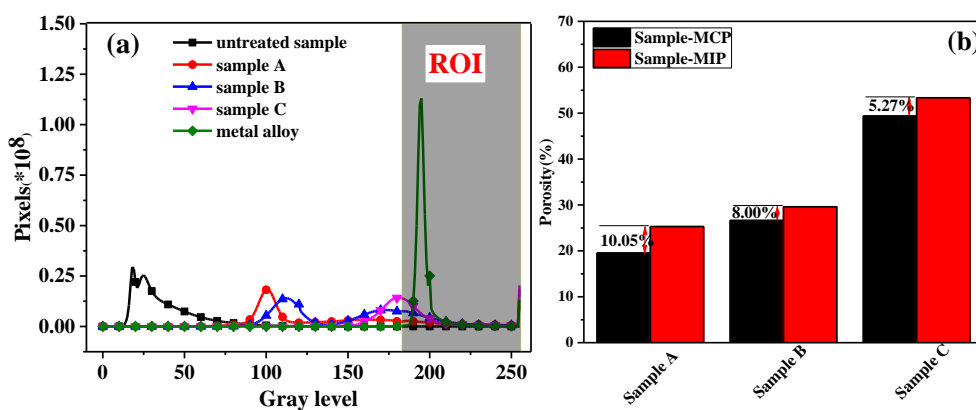
226

227 3.2 Porosity in 3D pore structure

228 As shown in Fig. 5a), gray level intensity was found to be the lowest in the
229 untreated sample and increased for the samples A, B, C and the metal alloy. This is
230 attributed to the fact that the gray level is closely related to the density and the
231 composition of sample [25]. The peak of the gray level in X-ray microtomography
232 image of the metal alloy was mainly composed of heavy metal elements (43.7%Bi,
233 20.6%Pb, 8.6%Sn, 5.8%Cd, 20.1%In, etc.), which was higher than that of the
234 untreated sample.

235 In 3D structure, greyscale 185~255 was chosen as ROI, which involved 0.08%
236 untreated sample and 97.09% the metal alloy greyscale, respectively. It's acceptable
237 that P_i was counted for sample A, B and C as 22.08%, 26.45% and 49.06% based on
238 ROI. Pixels ratio of the metal alloy on ROI was calculated as 97.09%, which was the
239 conversion coefficient ($\mu=0.9709$). P_a of 3D structure in sample A, B and C were
240 calculated for as 22.74%, 27.24% and 50.53%, which were consistent with values
241 obtained using MIP (25.28 %, 29.61% and 53.34%), as demonstrated in Table 4 and
242 Fig. 5 (b). Considering the results of MIP as references, the relative errors between the
243 proposed method and MIP were 10.05%, 8.00% and 5.27% for the tested samples,
244 which were found to be the highest in the sample A and decreased for sample B and C.
245 The porosity based on MCP was slightly lower than that determined by MIP, due to
246 pore wall breakage caused by high pressures when using MIP [8].

247



248

249

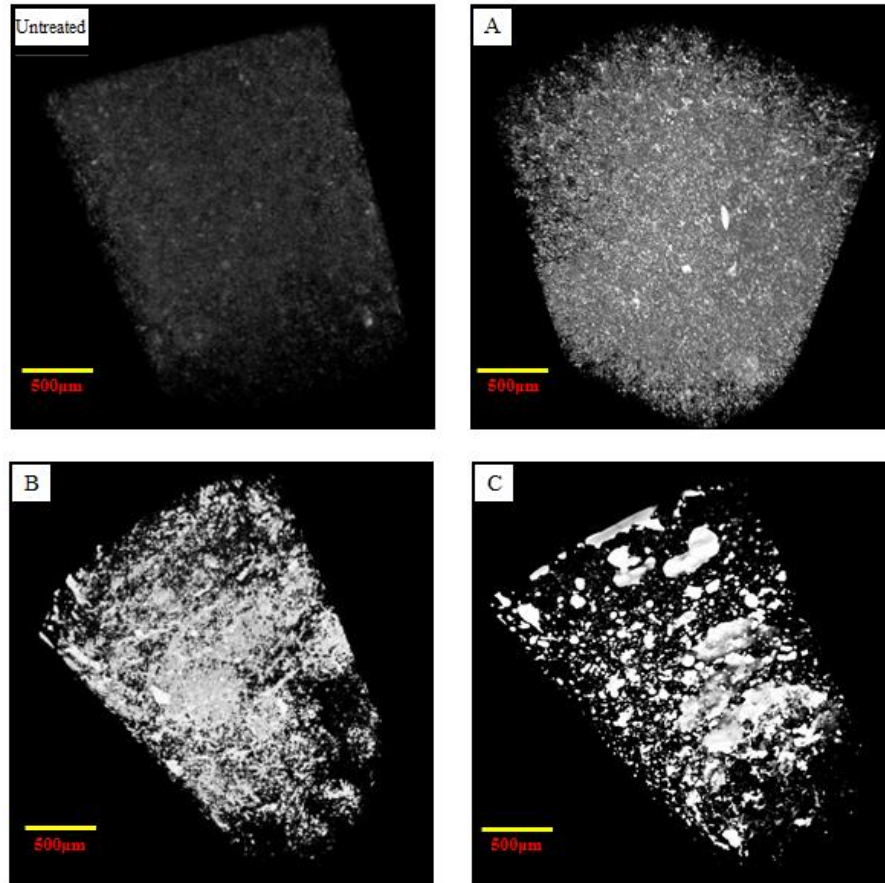
Fig. 5 Comparison of porosity between MCP and MIP

250 3.3 Reconstruction of 3D pore structure

251 In order to distinguish pore space and solid phase, the intruded samples (A, B and
252 C), untreated sample and the metal alloy were examined by X-ray microtomography

253 system under the same conditions. The threshold values of 184~255, 183~255 and
254 180~255 were chosen to distinguish the metal alloy (pore space) and cement when P_t
255 was very close to P_a , as shown in Fig. 6.

256



257

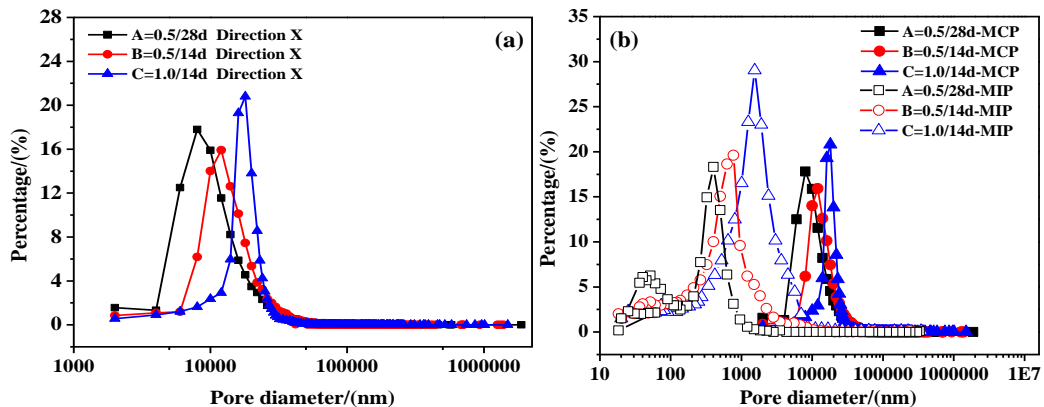
258 Fig. 6 The image of untreated sample and treated samples (A, B and C based on the threshold
259 of 184~255, 183~255 and 180~255)

260 3.4 Pore size distribution in 3D pore structure

261 The pore size distribution is an important parameter used to describe the
262 probabilities of different apertures in modern concrete. Considering the isotropy in
263 spatial distributions of porosity, sample A, B and C were visualized in direction X, as
264 shown in Fig. 7 (a). The smallest pore size was 2 μm because of the accuracy of
265 instrument, and the pore size distributions in the three directions were similar. The
266 most probable aperture decreased for sample A, B and C, in that order. This can be
267 attributed to the fact that lower w/c ratio can increase the density of the paste and
268 therefore reduce the pore space available for the metal alloy intrusion, similar to the
269 influence of a longer curing time [5].

270 Pore size calculated by MCP was compared with the results tested by MIP as
271 shown in Fig. 7(b). It is evident that the most probable aperture calculated by MCP

272 was greater than determined by MIP. Firstly, this can be partially explained by the
 273 heterogeneity of the pore structure in the cement-based material. The calculated
 274 direction of pore size by MIP is based on the volume of mercury entered, which
 275 strongly correlated with the metal-paste contact angle [25]. In other words, different
 276 aperture can be observed when the same one pore was researched in different
 277 observed direction. As for MIP, geometric surface of minimum-value aperture in the
 278 same pore space is preferentially filled by mercury, which named section pore size
 279 demonstrated in the vertical plane of pores [21, 25, 26]. Differently, one fixed direction [30]
 280 (direction X, Y or Z) of pore size investigated by MCP should be chosen for all pores
 281 before calculation, which strongly correlated with the selection of direction. Mostly,
 282 the pore size based on MCP is not minimum-value aperture in the same pore space,
 283 which named non- section pore size in the non-vertical plane of pores. From geometry
 284 considerations, the non-section dimension is larger than section dimension, which is
 285 analogous to the hypotenuse of a rectangular triangle being greater than the
 286 right-angle side. Secondly, the thresholding value based on images is the important
 287 factor to influence pore size distributions. Comparing with cement, the metal alloy is
 288 defined as pores space based on ROI combined with conversion coefficient. What's
 289 more, the minimum capillary pore radius that can be invaded by the molten metal
 290 alloy using the experimental set-up is $0.085\ \mu\text{m}$ and the smallest pore that could be
 291 distinguished by X-ray tomography is size of $2\ \mu\text{m}$, which directly generate that the
 292 pore size distribution will certainly be different from that provided by MIP. Therefore,
 293 the diameter (MCP) is longer than or equal to the diameter (MIP). Spatial distribution
 294 of porosity in cement-based materials is characterized by heterogeneity [30, 31].
 295



296
 297 Fig. 7 (a) Pore size distribution in X directions for 3D pore structure of sample A, B and C, (b)
 298 Comparison between MCP and MIP in the Pore size distribution from direction X
 299

300

301 **3. Conclusions**

302 X-ray microtomography combined with metal centrifugation porosimetry (MCP)
303 using a novel metal alloy, was applied for the first time to quantitatively investigate
304 3D pore structure in hardened cement paste. The contrast between pore space and
305 solid phase in X-ray microtomography imaging was improved due to the intrusion of
306 the low-melting-point metal alloy. A new threshold value segmentation method for
307 pore space was proposed based on ROI combined with conversion coefficient. The
308 porosity determined by MCP was close to MIP for the samples examined in this study
309 and the relative errors in the range of 5.27- 10.05 % were found in the values given by
310 MCP and MIP. It was established that the proposed MCP method is a powerful and
311 reliable technique for studying the 3D pore structures in cementitious materials, and it
312 could be speculated that future experiments could be carried out on the other materials.

313 **Acknowledgments**

314 Authors gratefully acknowledge the financial support National Natural Science
315 Foundation of China (51678143), 973 Program (2015CB655102) and National Key
316 R&D Program of China (2017YFB0309904).

317 **Data availability**

318 The raw/processed data required to reproduce these findings cannot be shared at this
319 time as the data also forms part of an ongoing study.

320 **References**

- 321 [1] Imbabi M S, Jones M R, Galvez J L, et al. Greening the construction industry:
322 Trends and developments in green cement and concrete technology[C].
323 International Sustainable Built Environment Conference. 2014.
- 324 [2] Taylor H F W. Cement Chemistry [J]. Chemistry for Engineers, 1992, 134.
- 325 [3] Abyaneh S D, Wong H S, Buenfeld N R. Computational investigation of capillary
326 absorption in concrete using a three-dimensional mesoscale approach[J].
327 Computational Materials Science, 2014, 87(5):54-64.
- 328 [4] Yang L, Zhang Y, Liu Z, et al. In-situ tracking of water transport in cement paste
329 using X-ray computed tomography combined with CsCl enhancing [J]. Materials
330 Letters, 2015, 160:381-383.
- 331 [5] Chen X, Wu S. Influence of water-to-cement ratio and curing period on pore
332 structure of cement mortar [J]. Construction & Building Materials, 2013, 38(6):

333 804-812.

334 [6] Nakashima Y. The use of X-ray CT to measure diffusion coefficients of heavy
335 ions in water-saturated porous media [J]. ENGINEERING GEOLOGY, 2000,
336 56(1-2): 11-17.

337 [7] Moro F, Břhni H. Ink-Bottle Effect in Mercury Intrusion Porosimetry of
338 Cement-Based Materials[J]. Journal of Colloid & Interface Science, 2002,
339 246(1):135-149.

340 [8] ZHOU J, PAN Y, CHEN X. Research Advances in Mercury Porosimetry Study
341 of Pore Structure in Cement-based Materials[J]. Material Review, 2013, 27(4):
342 72-75.

343 [9] Liu T, Zhang X, Li Z, et al. Research on the homogeneity of asphalt pavement
344 quality using X-ray computed tomography (CT) and fractal theory [J].
345 CONSTRUCTION AND BUILDING MATERIALS, 2014, 68: 587-598.

346 [10] Biqin Dong, Guohao Fang, Yuqing Liu, Peng Dong, Jianchao Zhang, Feng
347 Xing, Shuxian Hong. Monitoring reinforcement corrosion and corrosion-induced
348 cracking by Xray microcomputed tomography method. Cement and Concrete
349 Research, 100 (2017) 311–321.

350 [11] She W, Du Y, Zhao G, et al. Influence of coarse fly ash on the performance of
351 foam concrete and its application in high-speed railway roadbeds [J].
352 Construction & Building Materials, 2018, 170: 153-166.

353 [12] Liu G, Zhang Y, Wu M, et al. Study of depassivation of carbon steel in
354 simulated concrete pore solution using different equivalent circuits [J].
355 Construction & Building Materials, 2017, 157.

356 [13] Hsu J, Chen P, Huang K, et al. Efficiency of quantitative echogenicity for
357 investigating supraspinatus tendinopathy by the gray-level histogram of two
358 ultrasound devices[J]. JOURNAL OF MEDICAL ULTRASONICS, 2017,44(4):
359 297-303.

360 [14] Willis K L, Abell A B, Lange D A. Image-Based Characterization of Cement
361 Pore Structure Using Wood's Metal Intrusion[J]. Cement & Concrete Research,
362 1998, 28(12):1695-1705.

363 [15] Kaufmann J. Pore space analysis of cement-based materials by combined
364 Nitrogen sorption-Wood's metal impregnation and multi-cycle mercury
365 intrusion[J]. Cement & Concrete Composites, 2010, 32(7):514-522.

366 [16] Scrivener K L, Nematı K M. The percolation of pore space in the cement
367 paste/aggregate interfacial zone of concrete[J]. Cement & Concrete Research,

-
- 1996, 26(1):35-40.
- [17] G Desbois, S Hemes, B Laurich, et al. Investigation of microstructures in naturally and experimentally deformed reference clay rocks using innovative methods in scanning electron microscopy [J]. The Clay Minerals Society Workshop Lectures Series, 2016, 21:1-14.
- [18] Pyrak-Nolte L J, Montemagno C D, Nolte D D. Volumetric imaging of aperture distributions in connected fracture networks [J]. Geophysical Research Letters, 2013, 24(18): 2343-2346.
- [19] Hellmuth K H, Siitari-Kauppi M, Klobes P, et al. Imaging and analyzing rock porosity by autoradiography and Hg-porosimetry/X-ray computertomography -Applications[J]. Physics & Chemistry of the Earth Part A Solid Earth & Geodesy, 1999, 24(99):569–573.
- [20] Klobes P, Riesemeier H, Meyer K, et al. Rock porosity determination by combination of X-ray computerized tomography with mercury porosimetry[J]. Fresenius Journal of Analytical Chemistry, 1997, 357(5):543-547.
- [21] Washburn E W. Note on a Method of Determining the Distribution of Pore Sizes in a Porous Material [J]. Proceedings of the National Academy of Sciences of the United States of America, 1921, 7(4): 115-116.
- [22] L. MatWeb, Indium Corp. Indalloy 16 Low Melting Bismuth Alloy, MatWeb material property database, 2015.
- [23] L. MatWeb, Bi50-Pb26.7-Sn13.3-Cd10 Bismuth-Lead-Tin-Cadmium Fusible Alloy, MatWeb material property database, 2015.
- [24] Metals Handbook: Properties and Selection: Nonferrous Alloys and Special Purpose Materials, Vol. 2, 10th ed, ASM International. [Z].
- [25] Rakesh Kumar, B. Bhattacharjee. Study on some factors affecting the results in the use of MIP method in concrete research [J]. Cement and Concrete Research, 2003, 33: 417-424.
- [26] Rootare H M, Prenzlów C F. Surface areas from mercury porosimeter measurements [J]. Journal of Physical Chemistry, 1967, 71(8): 2733-2736.
- [27] Scrivener K L, Juilland P, Monteiro P J M. Advances in understanding hydration of Portland cement[J]. Cement & Concrete Research, 2015, 78:38-56.
- [28] A. Bazzoni, Study of early hydration mechanisms of cement by means of electron microscopy, Thèse EPFL n°296, 2014
(http://infoscience.epfl.ch/record/200217/files/EPFL_TH6296.pdf)
- [29] Lawrence F V, Young J F. Studies on the hydration of tricalcium silicate pastes

403 I. Scanning electron microscopic examination of microstructural features [J].
404 Cement & Concrete Research, 1973,3(2):149-161.

405 [30] Liu L, Wang X, Chen H, et al. Numerical modeling of drying shrinkage
406 deformation of cement-based composites by coupling multiscale structure
407 model with 3D lattice analyses [J]. Computers & Structures, 2017, 178: 88-104.

408 [31] Dong H, Sun J, Lin Z, et al. Three dimensional pore-type digital rock modeling
409 of natural gas hydrate for permafrost and numerical simulation of electrical
410 properties [J]. Journal of Geophysics & Engineering, 2018, 15: 275- 285.

411